Korean J. Chem. Eng., 35(1), 118-128 (2018)
DOI: 10.1007/s11814-017-0274-z

pISSN: 0256-1115
eISSN: 1975-7220

Model-based control of a molten carbonate fuel cell (MCFC) process

Tae Young Kim, Beom Suk Kim, Tae Chang Park, and Yeong Koo Yeo†

Department of Chemical Engineering, Hanyang University, Seoul 04763, Korea
(*Received 17 April 2017 • accepted 2 October 2017*)

Abstract−To improve availability and performance of fuel cells, the operating temperature of molten carbonate fuel cells (MCFC) stack should be strictly maintained within a specified operation range, and an efficient control technique should be employed to meet this objective. While most modern control strategies are based on process models, many existing models of MCFC are not ready to be applied in synthesis and operation of control systems. In this study, we developed an auto-regressive moving average (ARMA) model and machine learning methods of least squares support vector machine (LS-SVM), artificial neural network (ANN) and partial least squares (PLS) for the MCFC system based on input-output operating data. The ARMA model showed the best tracking performance. A model predictive control method for the operation of MCFC system was developed based on the proposed ARMA model. The control performance of the proposed MPC methods was compared with that of conventional controllers using numerical simulations performed on various process models including an MCFC process. Numerical results show that ARMA model based control provides improved control performance compared to other control methods.

Keywords: Molten Carbonate Fuel Cells, ARMA Modeling, Model Predictive Control, Rigorous Model

INTRODUCTION

A molten carbon fuel cell (MCFC) is well known to be an efficient clean energy generating facility. Among various types of fuel cell technologies, it is one of the readily available devices that are available in MW scale. A typical MCFC plant utilizes internal reforming of natural gas. This eliminates the need for a large external reformer to produce hydrogen fuel, resulting in the simple and compact plant configuration. In a typical MCFC system, chemical energy contained in fuel and oxidizer is converted to electric energy via electrochemical reaction. MCFC is considered to be one of the most promising candidates to replace the traditional fossil fuel burning thermal power plants which induce significant pollution emission. Recently, MCFC has evolved as a new generation of power source and relevant technology has been developed in large scale by many countries including United States, Europe, Japan and Korea.

So far modeling of MCFC processes has been focused on such issues as physical, chemical and transport properties, reaction kinetics, and static operation performance. From the operational point of view, simple expressions of fuel cells and balance-of-plant (BOP) are preferred for use in model-based control applications. Recently, several developments in the modeling of MCFC based on balance equations and specific assumptions have been reported. Effects of fuel cell geometry and complicated mass distributions on the plant performance have been taken into account in a rigorous model for external reforming MCFC systems [1,2]. Another rigorous model for internal reforming MCFC processes has been presented based on the assumptions of equilibrium chemical reactions and negligible mass accumulation [3]. A lumped-parameter model was reported based on both fast and slow process dynamics in reforming chemical reaction kinetics, mass accumulation, and losses due to the cell polarization [4]. Most of the proposed models developed so far employ mass, energy and momentum balance equations, resulting in process models too complicated to be used in the design of model-based control configurations. In general, the applicability of a rigorous model to design a model-based control scheme is restricted to adjustment of few operational conditions. Sheng [7] proposed a control method based on the steady-state optimization to give two coupled proportional-integral-derivative (PID) controllers. A large number of configurations and algorithms for identification and control based on artificial neural networks (ANN) have been proposed [6]. Shen et al. [7] proposed an adaptive neuro-fuzzy control method to control the temperature of MCFC stack using a model identified by ANN.

In this work, we propose a rigorous model, an auto-regressive moving average (ARMA) model, a least-square support vector machine (LS-SVM), an artificial neural network (ANN) model and a partial least squares (PLS) ed first to describe an MCFC plant. For the purpose of comparison, these models were used to analyze and to estimate dynamic behavior of the underlying MCFC plant. A model-based control method relies on the linearized process model, and the performance of a model-based control configuration based on the linearized rigorous model was analyzed and compared with that based on the linear ARMA model which is more compact and simpler than the LS-SVM model. Numerical simulations were performed to evaluate the response to the step changes in the set point.

PROCESS DESCRIPTION

Fig. 1 depicts the basic layout of the MCFC process including

†To whom correspondence should be addressed.
E-mail: ykyeo@hanyang.ac.kr

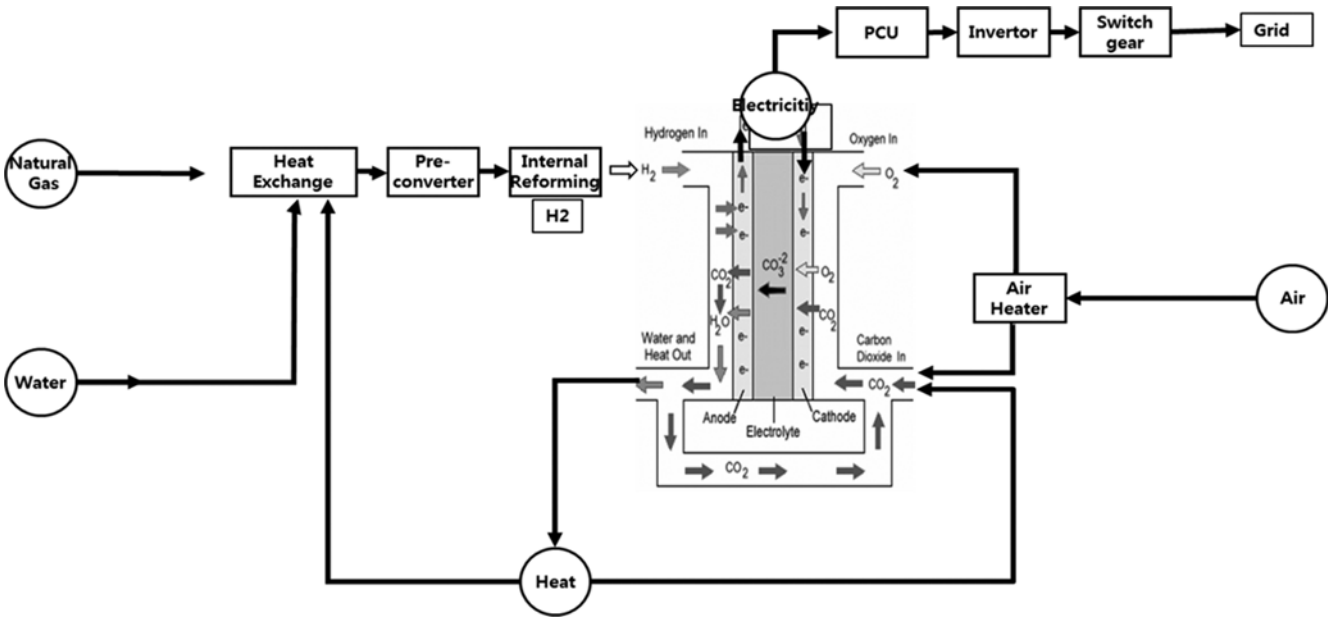

Fig. 1. Layout of the underlying MCFC process.

Table 1. Summary of the operating conditions of the MCFC process considered in this work

	Variables		Operating conditions	
Temperature (°C)	Anode inlet	Anode outlet	558-560	589-593
	Cathode inlet	Cathode outlet	552-565	537-546
Flow rate (kg/hr)	Anode inlet	Anode outlet	746-792	3,159-3,354
	Cathode inlet	Cathode outlet	11,486-12,197	9,070-9,631
Pressure (atm)	Anode inlet	Anode outlet	1.7-1.9	1.7-1.9
	Cathode inlet	Cathode outlet	1.7-1.9	1.7-1.9

the balance-of-plant (BOP) located in the suburban area of Seoul, Korea. Water is taken directly from the local municipal supply and then fed into a water purifier. Some of the water should be discharged to drain as part of the water purification processes, although in some applications this water can be collected for another purposes.

Fuel gas consists of steam and methane that is fed into the reforming units and anodes of the stack. Natural gas flows through two desulfurizers where sulfur compounds are removed to avoid damage to catalysts in the stack and pre-converter caused by these sulfur compounds. The majority of the desulfurized natural gas is transported to the humidifier where the gas is mixed with the water and is heated by cathode exhaust gases to form the fuel gas. The remainder of the natural gas is delivered to the air heater that acts as the primary electric air heater. The fuel gas formed by this procedure passes through the deoxidizer and the pre-converter that contains two types of catalyst. The first type of catalyst is the deoxidizer catalyst that is used to remove oxygen from the fuel gas by reaction with the methane. Some biogases and natural gas contain oxygen, which deactivates the nickel catalysts in the pre-converter and the fuel cell stack. The second type of catalyst is the nickel pre-converter catalyst to reform the fuel gas. The inlet gas temperature to the pre-converter is manipulated by skirting around some of the natural gas around the humidifier. The partially reformed fuel gas in the pre-converter flows to the stack. Within each fuel cell unit, the flow of the fuel gas splits equally to the four fuel cell stacks. Air is delivered to the fuel cell unit by the air blower. Initial heating of the units is achieved by the air to maintain proper oxidant temperature in the cathodes. As the flow of fuel gas increases, sufficient inlet hydrogen to the oxidizer is provided to heat the incoming air without assistance of the air heater. The operating conditions of the underlying MCFC process are summarized in Table 1.

The electrical-balance-of-plant (EBOP) (or the power conditioning system) includes the DC-to-AC inverter, the control system (commonly referred to as the power conditioning unit), the transformer(s), and the required switchgear. In addition to these, the EBOP contains the major electrical distribution equipment including breakers, transformers, and associated gears. The plant is connected to the electrical grid through the EBOP. When operating at lower power, the control system of the plant sends a DC current set point to the power conditioning unit based on the current that the fuel cell can support. The EBOP draws the DC current from the fuel cell followed by conversion to AC current.

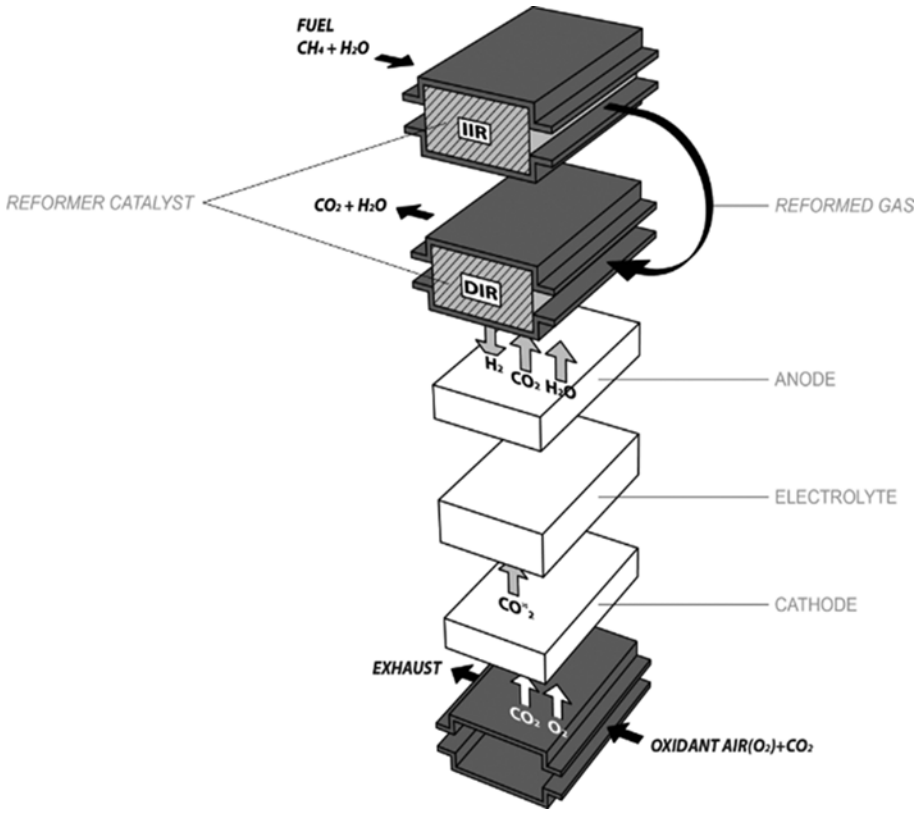

Fig. 2. IIR/DIR structure of MCFC stack.

MCFC PROCESS MODEL

1. Rigorous Model

In a typical MCFC process, natural gas is reformed to hydrogen in the internal reforming unit and the cells. Fig. 2 shows the two-step approach consisting of indirect and direct internal reforming (IIR and DIR) [8]. In the IIR step, a reforming unit is placed between every ten fuel cell units in the stack and converts about 50% of natural gas to hydrogen prior to enter into the cell anode. Further reforming occurs in the cell anodes (DIR step) that are loaded with reforming catalysts. The following electrochemical reactions are considered taking place in the MCFC process:

$$\text{Cathode: } CO_2 + \frac{1}{2}O_2 + 2e^- \rightarrow CO_2^{-2} \quad (1)$$

$$\text{Anode: } H_2 + CO_2^{-2} + 2e^- \rightarrow H_2O + CO_2 + 2e^- \quad (2)$$

$$\text{Total: } H_2 + O_2 \rightarrow H_2O + \text{Electricity} + \text{Heat} \quad (3)$$

Both of the following independent reactions occur in the IIR and the DIR step simultaneously:

$$\text{Reforming: } CH_4 + H_2O \rightarrow CO + 3H_2 \quad (4)$$

$$\text{Water-gas shift: } CO + H_2O \leftrightarrow CO_2 + H_2 \quad (5)$$

Actual performance (voltage) of the fuel cell for a specified load current is dependent upon the chemical reactants and products as well as the cell temperature. The voltage produced by an ideal hydrogen fuel cell operating at no load and room temperature (25 °C) is 1.229 V. As temperature increases, the ideal voltage decreases. This is because the energy available from the hydrogen-oxygen reaction becomes smaller as temperature increases. At the MCFC operating temperature (620 °C), the no-load voltage produced by the ideal fuel cell is just over 1 V. Since each stack operates under the same operating conditions, the rigorous model considers a lumped expression of all equivalent stacks. The reforming unit and the anode compartments are lumped together and are referred to as the anode hereafter. Anode and cathode are usually considered as two well-stirred compartments with mass (ions) interchange through the electrolyte (Na_2CO_3/Li_2CO_3) matrix separating the two compartments.

Temperatures of anode and cathode are nearly equal to each other, and elementary mole balances for each anode and cathode compartment can be represented as follows [9]:

$$V\tilde{C}_t \frac{dx_i}{dt} = N^{in}(x_i^{in} - x_i) - x_i \sum_{i=1}^{\xi} R_i + R_i, \quad i = 1, \ldots, \xi \quad (6)$$

where V is the volume of the compartment (m^3), $\tilde{C}_t$ is the total molar concentration (mol/m^3), N^{in} is the total molar flow into V (mol/s), x_i^{in} is the inlet mole fraction of component i, x_i denotes the mole fraction of component i, and ξ is the number of different species. R_i represents the rate of production of species i.

$$R_i = \sum v_{ij} r_i \quad (7)$$

where v_{ij} are the stoichiometric coefficients of species i in the reaction j (in the reforming reaction (4), H2 has a coefficient 3), and r_i is the molar extent of reaction (rate) in the reaction j.

Pressure dynamics at anode and cathode can be obtained by differentiating the equation of the ideal gas law with respect to time [10,11]. Mass balances in the anode and cathode can be given by

$$\frac{P_{an}V_{an}}{RT}\frac{dx_i}{dt} = N_{an}^{in}x_i^{in} - N_{an}^{out}x_i^{out} + \sum v_{ij}r_i \quad (8)$$

$$i_{anode} \in \{H_2, H_2O, CH_4, CO, CO_2, N_2\}$$

$$\frac{P_{ca}V_{ca}}{RT}\frac{dx_i}{dt} = N_{ca}^{in}x_i^{in} - N_{ca}^{out}x_i^{out} + \sum v_{ij}r_i \quad (9)$$

$$i_{cathode} \in \{H_2O, CO_2, O_2, N_2\}$$

The reaction rate in the cell follows the Faraday's law:

$$r_e = \frac{AJ}{2F} \quad (10)$$

where A is the cell area (cm^2), J is the current density (J/kg K), and F is the Faraday coefficient (J/mol V). The reaction rate in the reformer can be represented as follows [12]:

$$\text{Reforming: } r_s = Ak_s p_{CH_4}\exp\left(-\frac{E_A}{RT}\right) \quad (11)$$

$$EA = 82\ \text{kJ/mol}$$

$$\text{Water-gas shift: } r_w = Ak_w\left(1 - \frac{p_{H_2}p_{CO}}{p_{H_2O}p_{CO}K_w}\right)$$

$$K_W = \exp\left(\frac{4{,}276}{T} - 33.961\right) \quad (12)$$

where k_s and k_w are the rate constants for each reaction and K_W represents the equilibrium constant. E_A is activation energy. Electrical performance of the fuel cell in terms of temperature and gas compositions is given by the Nernst equation [13]

$$V_0 = E_0(T) + \frac{RT}{2F}\ln\frac{P_{H_2,a}P_{O_2}^{1/2}, c, P_{CO_2,c}}{P_{H_2O,a}P_{CO,a}} \quad (13)$$

where V_0 is the equilibrium potential (V) E_0 (T) the cell standard potential (V), and Pi the partial pressure of gas species i. The actual cell voltage is represented by the equilibrium cell potential and irreversible losses. The irreversible losses in the fuel cell are contributed by activation, concentration, and ohmic polarizations:

$$V_{cell} = V_0 - \eta_{act} - \eta_{conc} - iz \quad (14)$$

where V_{cell} is the cell voltage under load (V), η_{act} denotes the activation polarization (V), η_{conc} represents the concentration polarization (V), and z is the cell ohmic impedance ($\Omega\ cm^2$). The cell voltage, defined by Eq. (14), is an average value determined by bulk temperature and stack current, the anode side and cathode side pressures and gas compositions. The total stack voltage is obtained by multiplying the number of cells. Single cell experiments have been used to derive performance models for standard potential, activation polarization loss, concentration polarization loss, and ohmic loss. These models have been correlated to stack current density, average temperature, and average partial pressures of reactants and products. In the fuel cell stack model, the average temperature is taken as the arithmetic average of that of the cathode inlet and cathode exhaust. The average cathode partial pressure corresponds to the arithmetic average of the mole fractions at the cathode inlet and the cathode exhaust. Similar considerations apply to the anode; in this case, the mole fractions of the stream into the reforming unit (not into the anode) are taken as the anode inlet mole fractions (reforming unit and anode are assumed to be lumped). In the calculation of the anode inlet gas composition, it is assumed that both the water-gas shift reaction and the reforming reaction are at equilibrium. Eqs. (15)-(18) shown below summarize the dependencies of the terms appearing in the right hand sides of Eq. (13) and (14) on the single cell performance model.

$$E_0 = 4184[58.3 - 0.0113 + 9.6 * 10^{-7}T_c)T_c] \quad (15)$$

$$\eta_{act} = \frac{RT_c}{2F}(-21 - 0.31\ln P_{H_2,a} - 0.24\ln P_{CO_2,a} - 0.95\ln P_{H_2O,a} + 0.86\ln P_{CO_2,c} - 1.8\ln P_{O_2,c} + \frac{7050}{T_c} - 2.6\ln i) \quad (16)$$

$$\eta_{conc} = -1.22\ln\left(1 - \frac{i}{0.64}\right) \quad (17)$$

$$z = 0.4\exp\left[-2870\left(\frac{1}{923} - \frac{1}{T_c}\right)\right] \quad (18)$$

where T is the arithmetic average value of cathode inlet and outlet temperatures [K] and i is cell current [A/cm]. Anode and cathode partial pressures are taken as the arithmetic averages of inlet and exit gas partial pressures by assuming the anode inlet gas to be pre-equilibrated to account for the gas composition change within the reforming unit. Dynamics of the stack temperature can be represented by the following energy balance equation:

$$m_s\overline{C}_{ps}\frac{dT_s}{dt} = \sum \dot{n}_i^{in}\int_{T_{ref}}^{T_{in}} C_{p,i}(T)dT - \sum \dot{n}_i^{out}\int_{T_{ref}}^{T_s} C_{p,i}(T)dT - \dot{n}_{H_2}^{r}\Delta\hat{H}_r^o - V_{cell}I \quad (19)$$

where m_s and $\overline{C}_{ps}$ represent the mass and average specific heats of cell materials, respectively, $C_{p,i}$ is the specific heat of ith fuel or air entering the system, $\Delta\hat{H}_r^o$ is the specific heat of total reaction (3). The rigorous model for the MCFC process is compared with actual MCFC process operated with 50% load in Table 2. In the operation, the current density is 0.065 (A/cm^2) and the power is 1437.92 (kW).

Fuel utilization is defined as the fraction of total fuel fed into the cell that is consumed by electrochemical reactions:

$$U_f = \frac{H_{2,consumed}}{H_{2,in}} \quad (20)$$

where $H_{2,consumed}$ is the rate of consumption of hydrogen in the electrochemical reaction and $H_{2,in}$ is the molar flowrate of hydrogen into the fuel cell. For the internal reforming MCFC, $H_{2,in}$ is defined to account for internal generation of hydrogen:

$$H_{2,in} \equiv N_{ru}^{in}(x_{ru,H_2}^{in} + 4x_{ru,CH_4}^{in} + x_{ru,CO}^{in}) \quad (21)$$

Table 2. Comparison between the rigorous model and actual process with 50% load operation

	Voltage (V)	Stack temperature (°C)
Rigorous model	0.8834	614.75
Actual process	0.8813	615

This equation represents H_2 generated by (1) upstream reaction (pre-converter), (2) reforming reaction (reforming unit and cell), and (3) water-gas shift reaction (reforming unit and cell). The coefficient U_f in Eq. (20) follows from reactions (3) and (4). Faraday's law (9) can be used to replace $H_{2,\,consumed}$ by using the system DC current I_{sys} in the expression for fuel utilization. It is supposed that there are 4 model (258 cell per module) in 2.5 MW scale MCFC plant:

$$U_f=\frac{C_{total}I_{sys}}{2FH_{2,\,in}},\ C_{total}=4*258 \tag{22}$$

Steam-carbon ratio is simply defined as the molar ratio of steam to methane:

$$\text{s/c ratio}\equiv\frac{x_{H_2O}}{x_{CH_4}}=\frac{N_{H_2O}}{N_{CH_4}} \tag{23}$$

2. ARMA Model

The auto-regressive moving average (ARMA) model is adequate to interpret statistical time-series data and to estimate output values. In an auto-regression model, the variable of interest is forecasted using a linear combination of past data. The term "auto-regression" indicates that it is a regression of the variable against itself. An auto-regressive model of order p can be written as

$$X_t=\phi_1X_{t-1}+\phi_2X_{t-2}\ldots+\phi_pX_{t-p}+V_t \tag{24}$$

where V_t represents modeling error. This is a multiple regression with lagged values of X_t being used as predictors. This model is also referred to as an AR(p) model. Auto-regressive models are remarkably flexible at handling a wide range of different time series patterns. Rather than using past values of the forecast variable in a regression, a moving average model uses past forecast errors in a regression-like model:

$$V_t=w_t+\theta_1w_{t-1}+\theta_2w_{t-2}\ldots+\theta_qw_{t-q} \tag{25}$$

where w_t represents white noise.

This model is referred to as an MA(q) model. In the AR model, X_t can be thought of as a weighted moving average of the past few forecast errors. Combination of these two equations gives the model for X_t represented by ARMA (p, q) where p is the order of the auto-regressive part and q is the order of the moving average part. It can be seen that the ARMA model is static if the model is expressed as [14]:

$$X_t-\phi_1X_{t-1}-\cdots-\phi_pX_{t-p}=w_t+\theta_1w_{t-1}+\cdots+\theta_qw_{t-q}\quad wt\sim WN(0,\sigma^2) \tag{26}$$

We can abbreviate the Eq. (22) using the so-called backshift operator defined as $B_kX_t=X_{t-k}$. Using the B operator, Eq. (22) can be written as

$$\phi(z)X_t=\theta(z)w_t \tag{27}$$

where

$$\phi(z)=1-\phi_1z-\cdots-\phi_pz^p,\ \theta(z)=1+\theta_1z+\cdots+\theta_qz^q$$

The data of the air, water and natural gas flow rates in time are used to estimate values of coefficients in Eq. (23). The hydrogen flow involved in the reaction is used directly instead of the natural gas flow to evaluate the MCFC plant model. To calculate the hydrogen flow, it is assumed that 99% of the natural gas in a reformer is converted to hydrogen. The air, hydrogen and water flow rates are taken as manipulated variables (u_1, u_2, u_3) and the power, fuel utilization and s/c ratio are taken as controlled target variables to give the desired linear relation. Coefficients of the ARMA model were determined through recursive least square method.

The linear nature of the AR process allows one to express the governing equation for p+n data points of the process in the form of a classical least square problem as follows:

$$\begin{bmatrix}X[p+1]\\X[p+2]\\\vdots\\\vdots\\X[p+n]\end{bmatrix} \tag{28}$$

$$=\begin{bmatrix}X[p] & X[p-1] & \cdots & \cdots & X[0]\\X[P+1] & X[P] & \cdots & \cdots & X[1]\\ & \vdots & & & \\ & \vdots & & & \\X[P+n-1] & X[P+n-2] & \cdots & \cdots & X[n]\end{bmatrix}\begin{bmatrix}a_1\\a_2\\\vdots\\\vdots\\a_p\end{bmatrix}+\begin{bmatrix}w_{p+1}\\w_{p+2}\\\vdots\\\vdots\\w_{p+n}\end{bmatrix}$$

Eq. (28) can be rearranged by using vectors and matrices as

$$\mathbf{Y}_{n\times1}=\mathbf{A}_{n\times(p+1)}*\mathbf{X}_{(p+1)\times1}+\mathbf{w}_{n\times1} \tag{29}$$

By assuming **A** in (29) is full column rank, the least squares solution that minimizes the prediction error, or equivalently the noise vector $\mathbf{w}_{n\times1}$, can be easily obtained as

$$\mathbf{X}_{ls}=(\mathbf{A}^T\mathbf{A})^{-1}\mathbf{A}^T\mathbf{Y} \tag{30}$$

Thus, given a sufficient set of measurements **Y** such that **A** is full column rank, Eq. (30) gives an initial estimate of the AR model parameters a_1, a_2, … a_p. It is apparent that the estimates of the AR model parameters obtained above are random variable themselves and that these estimates improve as the number of data points (n) increases. The least squares estimation procedure described above can be easily modified to result in a recursive algorithm. The recursive least squares (RLS) method is frequently used in optimal estimations where measurements from sensors arrive sequentially: with each additional measured value, better estimates for the parameters or states under consideration are obtained. To incorporate the RLS method to dynamically adjust the parameters of the AR(p) model, we first assume that a set of n>>p measurements is obtained. With n measurements, Eq. (30) can be expressed in RLS form as

$$X_{ls}(n)=\left(\sum_{i=1}^{n}a_ia_i^T\right)^{-1}\sum_{i=1}^{n}y_ia_i \tag{31}$$

where a_i^T are the rows of **A** and y_i are the elements of **Y**. Initial values of P and q are given by

$$P(0)=\left(\sum_{i=1}^{n}a_ia_i^T\right) \tag{32}$$

$$q(0)=\sum_{i=1}^{n}y_ia_i \tag{33}$$

Table 3. Coefficients for the ARMA model for various target variables

Target variable \ Manipulated variable	Air flow (u_1)	Hydrogen flow (u_2)	Water flow (u_3)	Constant
Power	−0.2499	−0.9907	0.4128	0.8423
Fuel utilization	0.1681	0.7882	−0.6340	0.3386
Steam-carbon ratio	−0.1019	0.6961	1.0558	0.3979

where $P(0)\in\Re(p\times p)$ and $q(0)\in\Re(p\times 1)$. After initialization, each new sensor measurement can be added to matrix **A** and vector **Y**, and new values of P, q and X_{ls} are calculated by

$$P(n+1)=\lambda P(n)+a_{n+1}a_{n+1}^T \tag{34}$$

$$q(n+1)=\lambda q(n)+y_{n+1}a_{n+1} \tag{35}$$

$$X_{ls}(n+1)=P(n+1)^{-1}q(n+1) \tag{36}$$

According to Eqs. (34)-(36), addition of new measurements provides new estimates for the AR model parameters. The parameter $\lambda<1$ is a forgetting factor [15] which solves two shortcomings in the generic RLS algorithm. First, it weights each new measurement more heavily than the past values in calculating current values of P and q. Second, when $\lambda<1$, the intermediate values P and q are prevented from growing unbounded, thereby enabling a finite precession implementation of the RLS algorithm. It can be shown that if P(k) given by Eq. (34) for some k>0 is nonsingular, then P(k+r) is non-singular for all r>0. Table 3 shows coefficients for the ARMA model obtained for various target variables.

3. Least-squares Support Vector Machine (LS-SVM) Model

The support vector machine (SVM) was first introduced for classification and nonlinear function estimation and further investigated by many others [16]. The SVM for regression is formulated in solving a convex optimization problem, more specifically a quadratic programming (QP) problem. However, the major drawback of SVM is its higher computational burden because of the required constrained optimization programming. A major breakthrough has been obtained at this point with a least squares version of SVM, called LS-SVM. In LS-SVM [17,18], one works with equality instead of inequality constraints and a sum of squared error (SSE) cost function as it is frequently used in training of classical neural networks. This reformulation greatly simplifies the problem in such a way that the solution is characterized by a linear system. This linear system can be efficiently solved by iterative methods such as conjugate gradient.

Consider a given training set of N data points $\{x_k, y_k\}_{k=1}^N$ with input data $x_k\in\mathbf{R}^N$ and output $y_k\in r$ where $\mathbf{R}^N$ is the N-dimensional vector space and r is the one-dimensional vector space. The three input variables used for the LS-SVM model in this study are air flow (AF), hydrogen flow (HF), and water flow (WF): x=[AF, HF, WF]. The output (y) of the LS-SVM model is target variable (V_t) which may be voltage, utilization or steam to carbon ratio: $y=V_t$.

In feature space LS-SVM models take the form

$$y(x)=\mathbf{w}^T\varphi(x)+b \tag{37}$$

where the nonlinear mapping $\varphi(.)$ maps the input data into a higher dimensional feature space; $\omega\in\mathbf{R}^N$; $b\in r$; ω=an adjustable weight vector; b= the scalar threshold. In LS-SVM for function estimation the following optimization problem is formulated:

$$\text{Minimize: } \frac{1}{2}\omega^T\omega+\gamma\frac{1}{2}\sum_{k=1}^N e_k^2$$

$$\text{Subject to: } y(x)=w^T\varphi(x_k)+b+e_k,\ k=1,\ \ldots,\ N \tag{38}$$

where e_k is error variable and γ is regularization parameter. Smaller γ can avoid overfitting in case of noisy data. Note that there is an SSE fitting error and a regularization term in the cost function, which is also a standard procedure in the training of feedforward neural networks and is related to ridge regression.

The Lagrangian is given by

$$L_{LS\text{-}SVM}=\frac{1}{2}\|\omega\|^2+\gamma\frac{1}{2}\sum_{k=1}^N e_k^2-\sum_{k=1}^N\alpha_k\{\langle\omega,\ \varphi(x_k)\rangle+b+e_k-y_k\} \tag{39}$$

with Lagrange multipliers $\alpha_k\in R$. The optimality is given by

$$\begin{cases}\dfrac{\partial L_{LS\text{-}SVM}}{\partial\omega}=0\rightarrow w=\sum_{k=1}^N\alpha_k\varphi(x_k)\\ \dfrac{\partial L_{LS\text{-}SVM}}{\partial b}=0\rightarrow\sum_{k=1}^N\alpha_k=0\\ \dfrac{\partial L_{LS\text{-}SVM}}{\partial e_k}=0\rightarrow\alpha_k=\gamma e_k,\ (k=1,\ \ldots,\ N)\\ \dfrac{\partial L_{LS\text{-}SVM}}{\partial\alpha_k}=0\rightarrow\langle\omega,\ \varphi(x_k)\rangle+b+e_k-y_k=0\end{cases} \tag{40}$$

These conditions are similar to standard SVM optimality conditions, except for the condition $\alpha_k=\gamma e_k$, for which the sparseness property has been lost in LS-SVM.

After elimination of e_k, one obtains the following linear equations:

$$\begin{bmatrix}0 & 1_v^T\\ 1 & \Omega+I/\gamma\end{bmatrix}\begin{bmatrix}b\\ \alpha\end{bmatrix}=\begin{bmatrix}0\\ y\end{bmatrix} \tag{41}$$

where $y=[y_1;\ \ldots;\ y_N]$, $1_v=[1;\ \ldots;\ 1]$, $\alpha=[\alpha_1;\ \ldots;\ \alpha_N]$ and the Mercer condition has been applied again

$$\Omega_{kl}=\langle\varphi(x_k),\ \varphi(x_l)\rangle=K(x_k,\ x_l)\quad k,\ l=1,\ \ldots,\ N \tag{42}$$

Although the choices of the kernel function K(·,·) in LS-SVM are the same as those in SVM, more emphasis has been put on the powerful RBF kernel. The resulting LS-SVM model for function estimation becomes

$$VT=y(x)=\sum_{k=1}^N\alpha_k K(x,\ x_k)+b \tag{43}$$

where α and b are the solutions to Eq. (43), respectively and K(x, x_k) is the kernel function. The radial basis function has been used

as a kernel function in this analysis. The radial basis function is given by

$$K(x_k, x_l) = \exp\left\{-\frac{(x_k - x_l)(x_k - x_k)^T}{2\sigma^2}\right\},\ k=1, \ldots, N \tag{44}$$

where σ is the width of the radial basis function. In this study, the values of γ and σ^2 were obtained by bisection method. In this method, the iteration procedure is performed until the desired accuracy is reached:

$$|b_i - a_i| \le \varepsilon \tag{45}$$

where b_i and a_i are the upper and lower ends of the interval at the i^{th} iteration, respectively, and ε is the desired accuracy. Initial intervals for γ and σ^2 were set to [0.5 3] and [0.5 2], respectively. After some iterations, γ and σ^2 were found to converge to 1 and 1.2, respectively.

To be used in the derivation of LS-SVM model for the underlying MCFC plant, the operation data have been divided into two sub-sets: a training dataset, to construct the model, and a test dataset to validate the model performance. In this study, the training dataset consists of 8,411 data points and the test dataset consists of 4,320 data points. The data are scaled to locate within the range of [0 1], and the radial basis function given by Eq. (44) is used. The design values of the γ and σ are determined according to the procedure described above during the training of the LS-SVM model.

4. Artificial Neural Network (ANN) Model

An important aspect of ANN is that it may highly approach a nonlinear mapping of two different dimensional spaces [19]. Theoretically, it was already proved that a tri-layer feed forward network is capable of approximating any continuous functions by the free precision after training [20].

The sigmoid function is widely used for the actuating function of computation node of the network. In the ANN model, the input vector of the hidden layer $\{S_j\}$ is computed when the study sample A_k is fed into the input layer of the ANN model, and then the output vector of the hidden layer, namely $\{B_j\}$, is computed through the sigmoid function:

$$B_j = \sigma(S_j) = \sigma\left(\sum_{i=1}^{N} W_{ij} \cdot a_j - \theta_j\right) \tag{46}$$

where A_k is the input vector of the internal recurrent neural network (IRNN) model, W_{ij} is the connection weight of the input layer to the hidden layer and θ_j is the threshold of the output layer. Next, the input vector of the output layer $\{L_t\}$ is computed, and then the output vector of the output layer, $\{C_i^k\}$, is computed through the sigmoid function:

$$C_t^k = \sigma(L_t) = \sigma\left(\sum_{j=1}^{p} V_{jt} \cdot b_j - \gamma_t\right) \tag{47}$$

where γ_t is the threshold of the output layer and V_{jt} is the connection weight of the hidden layer to the output layer. The error of the network node is calculated backward according to the gradient drop law, and then the connection weights of the network are corrected through the accumulated error backward propagation. These procedures are repeated until the k groups of the pattern training are completed. The overall root-mean-square error of the whole network, E, is obtained as follows:

$$E = \sum_{k=1}^{m}\sum_{t=1}^{q}\sqrt{(y_t^k - C_t^k)^2} \tag{48}$$

where Y_k is the expected output vector of the ANN model. The output vector of the ANN with the bias node is given by:

$$Y(k) = \sum_{j=1}^{p} WO_j \cdot \sigma(S_j(k)) + WO_{bias} \tag{49}$$

$$S_j(k) = \sum_{i=1}^{p} WR_{ij} \cdot \sigma(S_j(k-1)) + \sum_{i=1}^{n} WI_{ij} \cdot I_{ij}(k) + WI_{jbias} \tag{50}$$

where WI, WR and WO are the weight coefficients of the input layer to the hidden layer, the feedback layer to the hidden layer and the hidden layer to the output layer, respectively, I is the input vector of the bias node and WI_{bias} and WO_{bias} are the weight coefficients of the bias node 1 to the hidden layer and the bias node 2 to the output layer, respectively.

In this study, the number of neurons in the hidden layer was determined by using the bisection method. For the range of the number of neurons in the hidden layer set to [5 9], the RMSE values of the voltage were within the range of [0.007 0.034], those of the fuel utilization were within the range of [2.81 3.30], and those of the steam to carbon ratio were within the range of [0.1395 0.1711]. The lowest values of RMSE were obtained when the number of neurons in the hidden layer was 7. The air flow, the hydrogen flow, and the water flow rates are used as the input variables for the ANN model, and the generation voltage, the fuel utilization and the steam to carbon ratio of the MCFC process are the output variables for the ANN model with seven neurons in the hidden layer. The data set consisting of 8,111 data points was used to train the ANN model and the data set consisting of 4,320 data points was used in the validation.

5. Partial Least Squares (PLS)

The partial least squares (PLS) method is a multiple linear regression model which can be used to model relations between inputs and outputs with correlations and/or restricted number of data points [21,22]. In the PLS method the high dimensional spaces of the input and output data acquired from a plant are projected onto the low dimensional feature spaces followed by identification of the best relationship between the feature vectors. More specifically, the high dimensional data matrices X and Y are projected onto several key factors (T, U) and linear regression is carried out for the relation between these factors. The outer relations for input block X and the output block Y are given by:

$$X = TP^T + E = \sum t_h \ p_h^T + E \tag{51}$$

$$X = UQ^T + F = \sum u_h \ q_h^T + F \tag{52}$$

The coefficient b_h combining each block can be found from the following relation:

$$\widehat{u_h} = b_h t_h \tag{53}$$

Usually, the least squares method is used to compute the regression coefficient $b_h\left(=\frac{u_h^T t_h}{t_h^T t_h}\right)$. In computation of key factors the non-

Table 4. Comparison of RMSE values

Target variable	Rigorous model	ARMA model	LS-SVM model	ANN model	PLS model
Voltage	0.0205	0.0035	0.0043	0.007	0.0068
Fuel utilization	13.1415	2.71	2.87	2.81	2.73
Steam-carbon ratio	0.0254	0.1304	0.3791	0.1395	0.2459

linear iterative partial least squares scheme is widely used as a computing algorithm. The nonlinear partial least squares method can be classified into two types: in type I, the inner relations among blocks are nonlinear and in type II, both the inner and outer relations are nonlinear. The general form of the type I is given by:

$$\widehat{u_h} = f(t_h) + R_h \tag{54}$$

Various models according to the function f have been proposed. For example, f can take a quadratic form or artificial neural network can be used.

6. Model Comparison

To compare the performance of the ARMA, LS-SVM, ANN and PLS models described above, values of RMSE for each model are computed as shown in Table 4. As can be seen in Table 4, the ARMA model exhibits the best estimation performance compared to LS-SVM, ANN and PLS models. This confirms the use of ARMA model in the analysis and model predictive control (MPC) design for the underlying MCFC process.

MODEL PREDICTIVE CONTROL OF MCFC PROCESS

1. PID Control

Proportional-integral (PI) and proportional-integral-derivative (PID) controllers are very effective control methods for the chemical industry, and it is well known that more than 95% of the controllers used in chemical process control operations are PI or PID type. The MCFC plant currently in operation also uses PID control. But, tuning control parameters (proportional coefficient, integral coefficient and differential coefficient) of these control types is very difficult, and it is not easy to achieve the optimal operation state under field conditions in the actual operation. It is difficult to determine suitable values especially for PID parameters without a systematic tuning procedure, which indicates that most of the PID controllers are poorly tuned in industrial applications. Moreover, conventional PI or PID controllers can hardly be sufficient enough in dealing with time delay, complex dynamics, or interactions. Embedding fuzzy method into these conventional controllers, or fuzzy controllers, may be a powerful alternative to overcome aforementioned problems and to enhance the control performance. The control command generated from the PID controller can be expressed in terms of proportional coefficient (K_P), integral coefficient (K_I), and derivative coefficient (K_D) as

$$u_{PID}(k) = K_P e + K_I * \int e\, dt + K_D \frac{de}{dt} \tag{55}$$

For example, the process rise time may be reduced by adjusting K_P, and the steady-state control error can be reduced by adjusting K_I [23].

2. Model Predictive Control Method

Model predictive control (MPC) method is an advanced, optimization based control strategy applicable to a wide range of industrial applications such as chemical plants and internal combustion engines. Future control inputs and future plant responses are estimated using a system model and optimized at regular intervals with respect to a performance. In this part, the ARMA and the rigorous model are used to implement the MPC. Using this models, the voltage, the steam to carbon ratio and the fuel utilization are predicted first. The cost function and constraints can be expressed as [24]:

$$\min_{U(k)} \frac{1}{2}\left(\|R - Y(k+1|k)\|_Q^2 + \|\delta U(k-1)\|_R^2 + \|v\|_S^2\right) \tag{56}$$

$$\begin{aligned} &Y_{min}(k+1) - v \le Y(k+1|k) \le Y_{max}(k+1) + v \\ &\delta U_{min}(k-1) \le \delta U(k-1) \le \delta u_{max}(k-1) \end{aligned} \tag{57}$$

where R, Y(k+1|k) and U(k) represent the set point, predicted output value and manipulated variable, respectively. To employ the rigorous model in MPC operation, the nonlinear rigorous model should be linearized since the MPC is based on the linear process model. The power (voltage) can be represented as

$$V_{cell} = V_0 - [R_a + R_c + R_{ir}]J \tag{58}$$

where V_0 is open circuit voltage, R_a and R_c are anode and cathode reaction resistances, respectively, and R_{ir} is internal resistance. Each of these variables can be given as following:

$$V_0 = \frac{4{,}184 * (58.3 - (0.0113 + 9.6 * 10^{-7}T)T)}{2F} + \frac{RT}{2F} \ln \frac{P_{H_2,a} P_{O_2,c}^{\frac{1}{2}} P_{CO_2,c}}{P_{H_2O,a} P_{CO_2,a}} \tag{59}$$

$$R_a = c_a e^{\frac{\Delta H_a}{RT}} P_{H_2,a}^{-0.5} \tag{60}$$

$$R_c = c_1 e^{\frac{\Delta H_{c_1}}{RT}} P_{O_2,c}^{-0.75} P_{CO_2,c}^{0.5} + c_2 e^{\frac{\Delta H_{c_2}}{RT}} P_{CO_2,c}^{-1} \tag{61}$$

$$R_{ir} = c_{ir} e^{\frac{\Delta H_{ir}}{RT}} \tag{62}$$

Substitution of Eqs. (60)-(62) into Eq. (58) gives

$$V_{cell} = V_0 - \left[c_a e^{\frac{\Delta H_a}{RT}} P_{H_2,a}^{-0.5} - \left(c_1 e^{\frac{\Delta H_{c_1}}{RT}} P_{O_2,c}^{-0.75} P_{CO_2,c}^{0.5} + c_2 e^{\frac{\Delta H_{c_2}}{RT}} P_{CO_2,c}^{-1} \right) - c_{ir} e^{\frac{\Delta H_{ir}}{RT}} \right] J \tag{63}$$

where c_i is the parameter related to electrodes and electrolytes, P is the pressure and ΔH is the enthalpy. The cell internal resistance varies with the ionic conductivity of the electrolyte and electrical conductivity of the plates. Assuming that voltage is a function of temperature and current density, Eq. (63) can be linearized as

$$\begin{aligned} V_{cell}(T, J) &\approx V_{cell}(T_s, J_s) + \left.\frac{dV_{cell}}{dT}\right|_{T_s, J_s}(T - T_s) + \left.\frac{dV_{cell}}{dJ}\right|_{T_s, J_s}(J - J_s) \\ &= V_{cell}(T_s, J_s) + \left[\frac{4184(0.0113 + 19.2 * 10^{-7} T_s)}{2F}\right. \\ &+ \frac{R}{2F}\ln\frac{P_{H_2, a} P_{O_2, c}^{\frac{1}{2}} P_{CO_2, c}}{P_{H_2O, a} P_{CO_2, a}} + \frac{C_a \Delta H_a}{RT_s^2} e^{\frac{\Delta H_a}{RT_s}} P_{H_2, a}^{-0.5} \\ &+ \left(\frac{C_1 \Delta H_{c_1}}{RT_s^2} e^{\frac{\Delta H_{c_1}}{RT_s}} P_{O_2, c}^{-0.75} P_{CO_2, c}^{0.5} + \frac{C_2 \Delta H_{c_2}}{RT_s^2} e^{\frac{\Delta H_{c_2}}{RT_s}} P_{CO_2, c}^{-1}\right) \\ &\left. - \frac{C_{ir} \Delta H_{ir}}{RT_s^2} e^{\frac{\Delta H_{ir}}{RT_s}}\right](T - T_s)J_s - \left[c_a e^{\frac{\Delta H_a}{RT_s}} P_{H_2, a}^{-0.5}\left(c_1 e^{\frac{\Delta H_{c_1}}{RT_s}} P_{O_2, c}^{-0.75} P_{CO_2, c}^{0.5}\right.\right. \\ &\left.\left. + c_2 e^{\frac{\Delta H_{c_2}}{RT_s}} P_{CO_2, c}^{-1}\right) - c_{ir} e^{\frac{\Delta H_{ir}}{RT_s}}\right](J - J_s) \end{aligned} \tag{64}$$

The fuel utilization defined by Eq. (20) can be linearized as

$$\begin{aligned} U_f &= U_f(I_{sys, s}, H_{2, in, s}) + \left.\frac{dU_f}{dI_{sys}}\right|_{I_{sys, s} H_{2, in, s}}(I_{sys} - I_{sys, s}) \\ &+ \left.\frac{dU_f}{dH_{2, in}}\right|_{I_{sys, s} H_{2, in, s}}(H_{2, in} - H_{2, in, s}) \\ &= 0.8 + 1.8310 * 10^{-4} * I_{sys} - 0.1095 * H_{2, in} \end{aligned} \tag{65}$$

The steam to carbon ratio given by Eq. (23) can be linearized as

$$\begin{aligned} SC &= SC(N_{H_2O, s}, N_{CH_4, s}) + \left.\frac{dSC}{dN_{H_2O}}\right|_{N_{H_2O, s} N_{CH_4, s}}(N_{H_2O} - N_{H_2O, s}) \\ &+ \left.\frac{dSC}{dN_{CH_4}}\right|_{N_{H_2O, s} N_{CH_4, s}}(N_{CH_4} - N_{CH_4, s}) \\ &= 2.5 + 0.0032 * N_{H_2O} - 0.0082 * N_{CH_4} \end{aligned} \tag{66}$$

where N_{H_2O} is the molar flow rate of water and N_{CH_4} is the molar flow rate of methane. The ARMA models used in the MPC are as follows:

$$Y(x) = -\frac{0.2499}{z} u_1(z) - \frac{0.9907}{z} u_2(z) + \frac{0.4128}{z} u_3(z) \tag{67}$$

In the MPC simulations, the voltage, the steam to carbon ratio and the fuel utilization data obtained from the MCFC plant operation serve as the set point of the step changes.

3. Control Simulations

Simulations of PID and MPC operations are performed using the MATLAB/Simulink platform. Step responses of the voltage are obtained through the MPC simulations using the linearized rigorous model and the ARMA model. Input data used in the MPC simulations are shown in Fig. 3. Fig. 3(a) shows the up-step changes and Fig. 3(b) shows the down-step changes in the input flow rates.

Fig. 4 shows the responses of the voltage obtained from the simulations of PID and MPC based on the linearized rigorous model and the ARMA model. Fig. 4(a) displays the up-step responses, Fig. 4(b) displays the down-step responses, and Fig. 4(c) displays responses for the multiple step changes in inputs. The MCP results based on the ARMA model show 98.6% improvement in the up step, 98.1% in the down step, and 98.4% in the multiple step changes compared to those based on the rigorous model. Table 5 shows the settling times in the PID control and MPC based on the rigorous and ARMA models. We can see that the settling time in the MPC based on the rigorous model is more than 50 seconds for the case of up-step and down step, and more than 200 seconds for the case of multiple step changes. This means that the MPC operation based on the rigorous model is not suitable for the underlying MCFC process. In contrast to the MPC based on the rigorous model, both

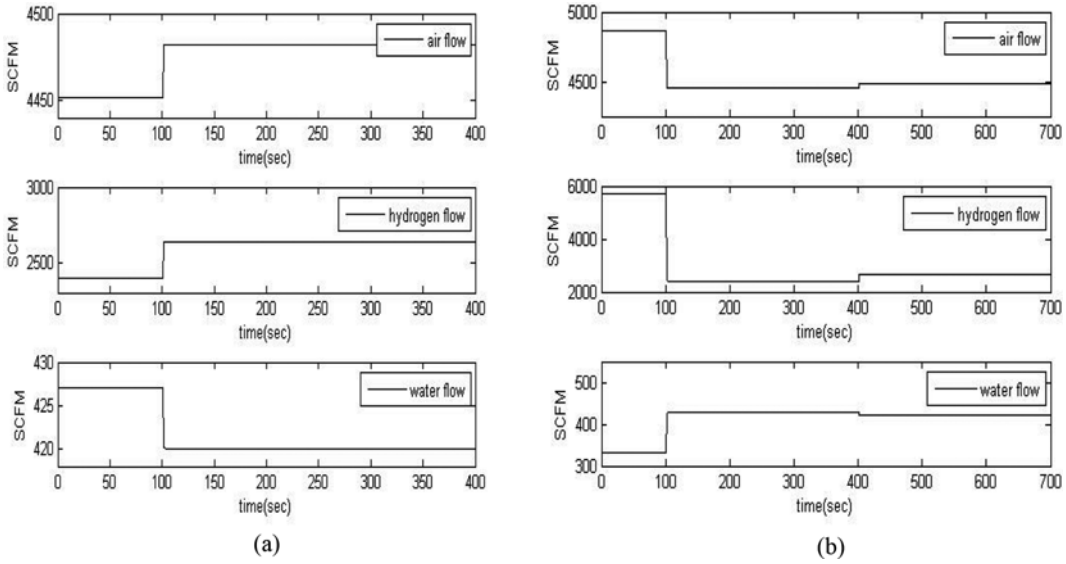

Fig. 3. Input flow rate data used in the simulation of MPC using rigorous and ARMA models: Up-step (a) and down-step (b).

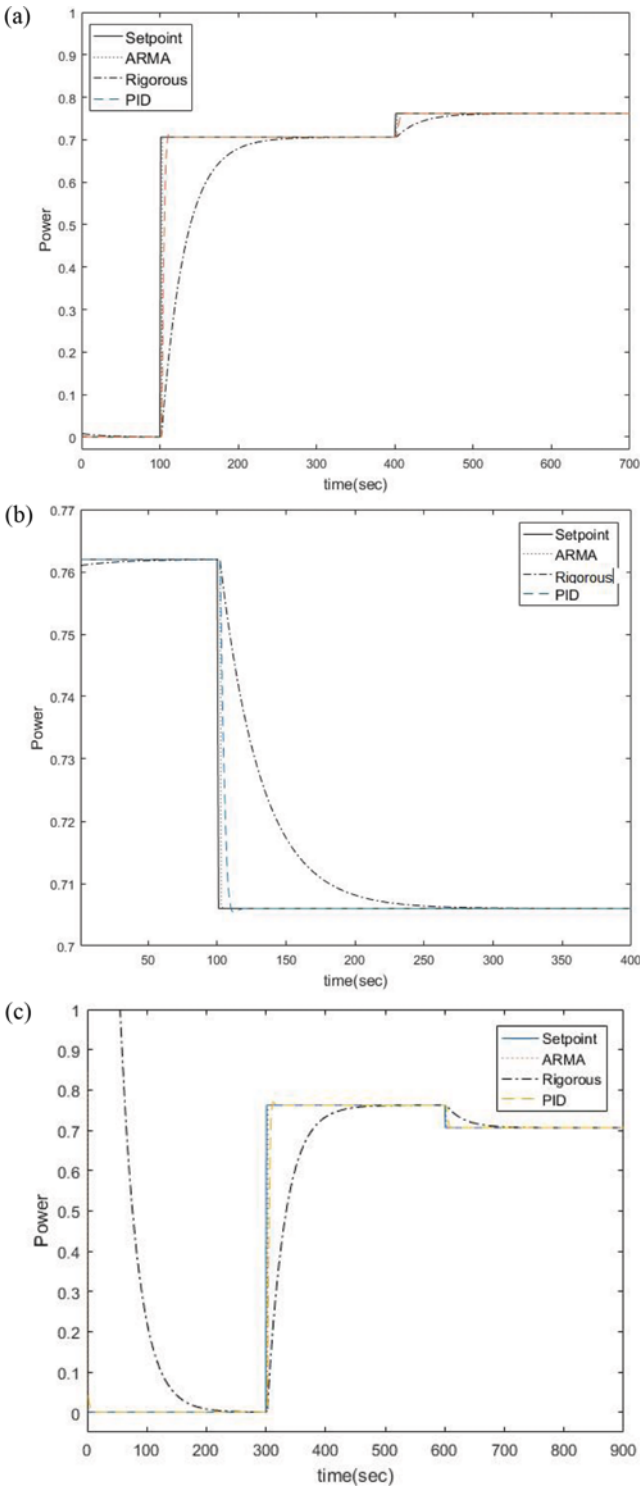

Fig. 4. Results of control simulations for voltage using PID and MPC based on rigorous and ARMA models: (a) Up-step; (b) down-step; (c) multiple step changes.

the PID and MPC based on the ARMA model reach the set point within couple of seconds. This implies the MPC based on the ARMA model is suitable for actual operation. The results of the MPC operation based on the ARMA model show 80% improvement in the up step setpoint changes, 78.9% in the down step setpoint changes, and 77.7% in the multiple step changes in the setpoint compared to the PID used in the actual MCFC plant.

Table 5. Comparison of the settling time between PID control and MPC based on the rigorous and ARMA models

	MPC based on ARMA model	MPC based on rigorous model	PID control
Up step	4	289	20
Down step	4	213	19
Step Change	4	255	18

CONCLUSIONS

The output voltage, the steam-to-carbon ratio and the fuel utilization are important controlled variables in the operation of an MCFC system. However, these target variables are rather complicated nonlinear functions of the current density, the natural gas being used as fuel and the air flow, indicating that nonlinear control scheme is required to adequately regulate the target variables for parameter changes. To assess and choose the model to be used in the model predictive control system, a rigorous model, ARMA model, LS-SVM model and ANN model are presented and compared with each other based on the plant operation data. For each target variable, the ARMA model exhibits the best tracking performance. The MPC scheme using the linearized rigorous model and the ARMA model are configured and tested numerically. It turns out that the MPC method based on the ARMA model shows better control performance compared to the PID control and MPC based on the linearized rigorous model. The control performance of the proposed ARMA model predictive control methods is compared with that of MPC based on the linearized rigorous model and conventional PID controller using numerical simulations performed on various process models including a MCFC process. Simulation results show that the ARMA model predictive control provides improved control performance than other control methods, especially for the MCFC process. The rigorous model was found to be not suitable to be used in MPC operation because of the slow response time compared to the MPC based on ARMA model. The MPC based on the ARMA model exhibited improved control performance compared to other control methods in terms of response speed for various step changes.

ACKNOWLEDGEMENTS

This work was supported by Korea Research Foundation Grant funded by the Korean Government (NRF-2017R1A2B1005649).

NOMENCLATURE

A : area of the cell [cm^2]
c_i : parameter related to electrodes and electrolytes
$\tilde{C}_t$: total molar concentration [mol/m^3]
$C_{p,i}$: specific heat of ith fuel or air gas entering the system [kJ/kg K]
$\overline{C}_{ps}$: specific heat of fuel cell materials excluding gases [kJ/kg K]

E_0 : cell standard potential [V]
F : faraday coefficient [J/mol V]
$H_{2,consumed}$: rate of consumption of hydrogen in the electrochemical [mol/s]
$H_{2,in}$: molar flowrate of hydrogen in the fuel cell [mol/s]
$\Delta\widehat{H}_r^o$: enthalpy of total reaction of equation [kJ/mol]
K_P : proportional coefficient
K_I : integral coefficient
K_D : derivative coefficient
i : cell current density [A/cm^2]
I : system current [A]
J : current density [A/cm^2]
k_s : rate constants for reforming reaction
k_w : rate constants for water gas shift reaction
K_w : equilibrium constant for water gas shift reaction
m_s : mass of fuel cell materials excluding gases [kg]
N^{in} : total molar flow into volume V [mol/s]
N_a^{in} : inlet molar flow in anode [mol/s]
N_c^{in} : inlet molar flow in cathode [mol/s]
N_{ru}^{in} : RU inlet total molar flow [mol/s]
N_a^{out} : outlet molar flow in anode [mol/s]
N_c^{out} : outlet molar flow in cathode [mol/s]
P : total gas pressure [kg/m s^2]
P_a : pressure in anode [kg/m s^2]
P_c : pressure in cathode [kg/m s^2]
P_{CH_4} : partial pressure of CH_4 [kg/m s^2]
P_{CO} : partial pressure of CO [kg/m s^2]
P_{H_2} : partial pressure of H_2 [kg/m s^2]
P_{H_2O} : partial pressure of H_2O [kg/m s^2]
$P_{CO_2,a}$: partial pressure of C_2O in anode [kg/m s^2]
r_0 : internal resistance [Ω cm^2]
r_j : rate of reaction j [mol/L s]
r_s : rate of reforming reaction [mol/L s]
r_w : rate of water gas shift reaction [mol/L s]
R : universal gas constant [J/mol K]
R_i : total production rate of species [mol/s]
s/c ratio : steam to carbon ratio
T_0 : ambient temperature [K]
T_S : stack temperature [K]
T_c : cathode inlet and outlet average temperature [K]
U_f : fuel utilization
V : compartment volume [m^3]
V_0 : equilibrium cell potential [V]
V_a : anode compartment volumes [m^3]
V_c : cathode compartment volumes volume [m^3]
V_{cell} : stack voltage [V]
x_i : mole fraction of gas species i
x_i^{in} : inlet mole fraction of gas species i
x_{ru,CH_4}^{in} : RU inlet gas mole fractions of CH_4
$x_{ru,CO}^{in}$: RU inlet gas mole fractions of CO
x_{ru,H_2}^{in} : RU inlet gas mole fractions of H_2
x_i^{out} : outlet mole fraction of gas species i
z : cell ohmic impedance [Ω cm^2]
η_{act} : activation polarization [V]
η_{conc} : concentration polarization [V]
v_{ij} : stoichiometric coefficients of species i in reaction j

REFERENCES

1. W. He, *J. Power Sources*, **52**, 179 (1994).
2. W. He, *J. Power Sources*, **55**, 25 (1995).
3. J. B. Ernest, H. Ghezel-Ayagh and A. K. Kush, Proceedings of the 1996 fuel cell seminar, Orlando, FL, U.S.A., 75 (1996).
4. M. D. Lukas, K. Y. Lee and H. Ghezel-Ayagh, *IEEE Trans. Energy Conver.*, **14**(4), 1651 (1999).
5. A. Comite, C. Costa, R. Di Felice, P. Paglia and D. Vitiello, *Korean J. Chem. Eng.*, **32**(2), 239 (2015).
6. C. Gu, C. Zhang, X. Zhang, N. Ding, B. Li and Z. Yuan, *Korean J. Chem. Eng.*, **34**(1), 20 (2017).
7. M. Sheng, M. Mangold and A. Kienle, *J. Power Sources*, **162**, 1213 (2006).
8. C. Shen, G.-Y. Cao and X.-J. Zhu, *Simulation Modeling Practice and Theory*, **10**, 109 (2002).
9. C. Shen, G.-Y. Cao, X.-J. Zhu and X.-J. Sun, *J. Process Control*, **12**, 831 (2002).
10. M. Farooque, H. C. Maru and B. Baker, Proceedings of the 28th Intersociety Energy Conversion Engineering Conference, Atlanta, GA, U.S.A., 181 (1993).
11. M. D. Lukas, K. Y. Lee and H. Ghezel-Ayagh, *Control Engineering Practice*, 197 (2002).
12. M. D. Lukas, K. Y. Lee and H. Ghezel-Ayagh, Proceedings of the 2000 IEEE power engineering society summer meeting, Seattle, WA, U.S.A., 1793 (2000).
13. M. D. Lukas and K. Y. Lee, *Fuel Cells.*, **5**(1), 115 (2004).
14. AKM M. Murshed, Biao Huang and K. Nandakumar, *J. Power Sources*, **163**, 830 (2007).
15. J. H. Hirschenhofer, D. B. Stauffer, R. R. Engleman and M. G. Klett, Fuel Cell Handbook, U.S. Department of Energy (1998).
16. S. E. Said, D. David and A. Dickey, *Biometrika*, **71**(3), 599 (1984).
17. H. Monson, Statistical Digital Signal Processing and Modeling, Jone Wiley & Sons., New York, U.S.A., 541 (1996).
18. J. A. K. Suykens, *Proceeding of IEEE Instrumentation and measurement technology*, Budapest, Hungary, 287 (2001).
19. P. Samui, *Scientific Research*, 431 (2011).
20. H. Wang and D. Hu, *IEEE*, 279 (2005).
21. M. T. Hagan, H. B. Demuth and M. H. Beale, Boston, MA: PWS Publishing Company (1996).
22. Y. D. Tian, X. J. Zhu and G. Y. Cao, *J. University of Science and Technology Beijing*, **12**, 72 (2005).
23. S. Thamizmani and S. Narasimman, *Int. J. Emerging Res. in Management Technology*, **3**(4), 66 (2014).
24. J. K. Lee and S. W. Park, *Korean J. Chem. Eng.*, **8**(4), 195 (1991).